


# Optically Controlled Valley Filter and Transistor Based on Transition-Metal Dichalcogenide Planar Heterojunctions

Laipeng Luo<sup>✉</sup>, Shengxiang Wang<sup>✉</sup>, and Yong Guo<sup>\*</sup>

*Department of Physics and State Key Laboratory of Low-Dimensional Quantum Physics, Tsinghua University, Beijing 100084, People's Republic of China*

 (Received 8 May 2022; revised 4 August 2022; accepted 23 August 2022; published 7 October 2022)

In this work, we theoretically explore the spin- and valley-resolved transport in monolayer transition-metal dichalcogenide (TMDC) planar heterojunctions. We propose two types of MoS<sub>2</sub>/WS<sub>2</sub> planar heterojunctions based on the position of the optical modulation. Spin- and valley-resolved transmission is realized and transmission spectra look quite different between the two types of heterojunctions due to the spin-valley-dependent effective potential, which results from the off-resonant circularly polarized light (CPL) and the band offset. Specifically, fully valley-polarized transport is demonstrated in Type-1 heterojunction (optical modulation on WS<sub>2</sub>). However, transmission in Type-2 heterojunction (optical modulation on MoS<sub>2</sub>) experiences a dramatic change with respect to CPL intensity, where the system can be switched from perfect valley-polarized “on” state to nearly nonpolarized “off” state only by adjusting the CPL intensity. As a result, we propose pure optically controlled valley filter and valley transistor based on the two types of planar heterojunctions, respectively. This work may shed light on potential application of valleytronic devices based on TMDC planar heterojunctions.

DOI: [10.1103/PhysRevApplied.18.044020](https://doi.org/10.1103/PhysRevApplied.18.044020)

## I. INTRODUCTION

Transition-metal dichalcogenides (TMDCs) have attracted extensive attention due to their possible application for next-generation devices [1,2]. TMDCs have several unique advantages, such as considerable energy gap in the visible frequency range [3,4] and strong spin-orbit coupling (SOC) originating from the *d* orbital of transition metal atoms [5]. In monolayer TMDCs, the broken inversion symmetry together with strong SOC leads to coupling between spin and valley degrees of freedom, resulting in valley-dependent spin splitting of the valence band [6]. In addition, there are two inequivalent valleys located at the corners of hexagonal Brillouin zone in TMDCs, which are connected with time-reversal symmetry [7,8]. Therefore, TMDCs are an important platform for research on spin and valley physics.

Controlling electrons with a specific spin or valley is a fundamental issue in spintronics and valleytronics [9]. Several modulation methods have been proposed and realized in both theoretical and experimental research based on TMDCs. For example, in the ferromagnetic MoS<sub>2</sub> junction, perfect spin and valley polarization as well as a controlled tunneling magnetoresistance effect can be realized with an applied gate voltage [10,11]. Due to broken inversion symmetry, monolayer TMDCs exhibit valley-dependent optical interband excitation, where circularly

polarized light (CPL) with different helicity selectively excites electrons in different valleys [12]. Quantum spin and valley Hall effects are predicted in off-resonant CPL-illuminated MoS<sub>2</sub> [13]. In addition, valley-polarized transport has been observed in optically pumped MoS<sub>2</sub> [14–16]. As the case in graphene [17], spin and valley filter/valve based on WSe<sub>2</sub> heterostructures have also been theoretically proposed [18,19].

A planar heterojunction (PH) is an important kind of two-dimensional (2D) material heterostructure, in which different 2D atomic panels are combined in a single atomic layer because of the similar structure and relatively small lattice mismatch. Previous studies mainly focused on heterogeneous junctions, such as hBN-graphene [20], or homogeneous junctions like zigzag-graphene/armchair-graphene nanoribbons with different sizes and edges to form metal-semiconductor heterojunctions [21,22]. Since TMDC materials in 2H phase (for example, MX<sub>2</sub>; *M* = Mo/W, *X* = S/Se) are very similar in their atomic structure, the planar heterojunctions can share atomically flat interfaces, where a localized edge state is predicted due to the hybridization of orbitals [23]. Band offset [24,25] between different components of PHs can be utilized to modify the electronic properties, which makes them valuable in the design of potential functional devices. For example, the band offset in planar heterojunctions facilitates the spatial separation of electrons and holes, which improves the light absorption and detection efficiency [26]. Enhanced thermoelectrical performance

\*guoy66@mail.tsinghua.edu.cn

has also been proposed in PH superlattices [27]. Since 2014, several experimental groups have successfully synthesized atomically flat TMDC PHs [28–30], which can be divided into three categories: (1) PHs with shared  $M$  atom, such as  $\text{MoS}_2/\text{MoSe}_2$ ; (2) PHs with common  $X$  atom, such as  $\text{MoS}_2/\text{WS}_2$ ; and (3) PHs with different  $M$  and  $X$  atoms. It has been demonstrated that those with common  $X$  atoms have the smallest lattice mismatch ( $< 1\%$ ) [29,31,32], where the effect of strain on the interface can be neglected. In contrast, in the PHs with different  $X$  atoms, the lattice mismatch is about 4% [28], which leads to sizable strain and lattice relaxation effects should be considered [33].

In this work, we focus on TMDC planar heterojunctions with shared  $X$  atom for the negligible strain effect on the interface, and we perform numerical calculations on spin and valley transport in  $\text{MoS}_2/\text{WS}_2$  planar heterojunctions with off-resonant circularly polarized light. We define two types of structures based on the position of the CPL modulation: Type-1 structure with the optical modulation on the  $\text{WS}_2$  region and Type-2 structure with the optical modulation on the  $\text{MoS}_2$  region [see Figs. 1(a) and 1(c)]. Figures 1(b) and 1(d) show the relative energy offset of the conduction band minimum (CBM) in the two types of heterojunctions. The band alignment and relative CBM energy of pristine monolayer  $\text{MoS}_2$  and  $\text{WS}_2$  are obtained by first principles calculations according to previous theoretical research [24]. The CPL irradiation greatly modifies the relative energy offset in the heterojunctions. The band offset between  $\text{MoS}_2$  and  $\text{WS}_2$  also plays an important role in quantum transport, which acts as an effective “barrier” or “well” when electrons tunnel through the heterojunctions. Considering the dispersion of the energy bands, these barriers or wells are sensitive to the incidence angle and energy, which results in quite different tunneling behaviors. As a result, we demonstrate a pure optically controlled valley filter based on Type-1 heterojunction because of the CPL-controlled perfect valley polarization, and an optically controlled valley transistor based on Type-2 heterojunction due to the dramatic change of valley-resolved transmission as a function of CPL intensity.

## II. MODEL AND METHODS

In this context, we denote electrons with spin up and spin down as  $\uparrow$  and  $\downarrow$ , respectively, and those with different valleys as  $K$  and  $K'$ . In normal regions, the low-energy effective Hamiltonian of a monolayer TMDC can be described by [5]

$$\hat{H} = a\tau(\eta k_x \hat{\sigma}_x + k_y \hat{\sigma}_y) + \frac{\Delta}{2} \hat{\sigma}_z - \lambda \eta \frac{\hat{\sigma}_z - 1}{2} \hat{s}_z, \quad (1)$$

where  $\sigma_i$  is the Pauli matrix,  $a$  is the lattice constant, and  $\tau$  represents the coupling between the states at the band

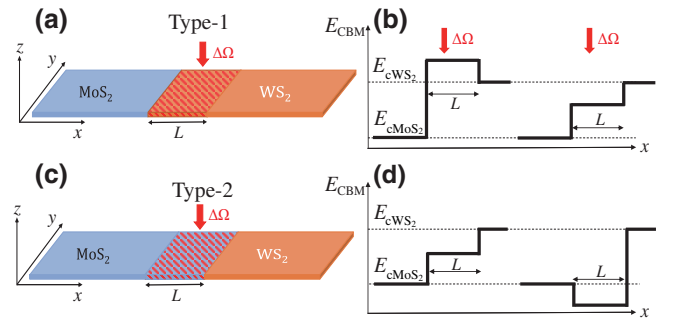


FIG. 1. Schematic diagram of Type-1 (a) and Type-2 (c) heterojunctions. The blue and orange regions represent  $\text{MoS}_2$  and  $\text{WS}_2$ , respectively. The red shaded area denotes the optical modulation region with length  $L$ . The relative energy offset (band alignment) in Type-1 (b) and Type-2 (d) heterojunctions.  $K$  valley (left part) and  $K'$  valley (right part). Electrons are injected along the positive  $x$  direction, and  $L$  is the length of the modulated region.

extrema in the  $\mathbf{k} \cdot \mathbf{p}$  approximation.  $2\lambda$  is the spin splitting at the valence band top caused by SOC and  $\Delta$  is the energy gap.  $s_z = 1$  ( $-1$ ) represents spin up (down) electrons and  $\eta = 1$  ( $-1$ ) corresponds to  $K$  ( $K'$ ) valley. In optical modulation regions, the TMDC is illuminated with circularly polarized light, which can be described by an electromagnetic potential as  $A(t) = [A \sin(\pm\Omega t), A \cos(\pm\Omega t)]$ , where  $A$  and  $\Omega$  correspond to the amplitude of potential and frequency of light, respectively. Based on the Floquet theory [34], when  $\hbar\Omega \gg \tau$ , the effect of time-dependent electromagnetic potential on the system can be reduced to an effective static Hamiltonian. The circularly polarized light does not directly excite the electrons and instead effectively modifies the electronic structure through virtual photon absorption and emission processes [35,36]. When  $eAv_f/\hbar\Omega \ll 1$ , the effective static Hamiltonian near the Dirac point can be written as  $\pm\eta\Delta\Omega\sigma_z$ , where  $\Delta\Omega$  is the effective energy term describing the intensity of the CPL. Therefore, in the modulated region, the effective Hamiltonian is

$$\hat{H} = a\tau(\eta k_x \hat{\sigma}_x + k_y \hat{\sigma}_y) + \frac{\Delta}{2} \hat{\sigma}_z - \lambda \eta \frac{\hat{\sigma}_z - 1}{2} \hat{s}_z \pm \eta \Delta \Omega \hat{\sigma}_z, \quad (2)$$

where  $\Delta\Omega = (eAv_f)^2/\hbar\Omega$ , and  $+$  ( $-$ ) corresponds to right-handed (left-handed) circularly polarized light. The general form of the wave function in each region is

$$\Psi(x) = a \left( \frac{1}{\sqrt{K_c/K_v}} e^{i\eta\theta} \right) e^{ik_x x} e^{ik_y y} + b \left( \frac{1}{-\sqrt{K_c/K_v}} e^{-i\eta\theta} \right) e^{-ik_x x} e^{ik_y y}, \quad (3)$$

$$K_c K_v = k_x^2 + k_y^2 = \mathbf{k}^2. \quad (4)$$

Here we define  $K_c = (E - E_c - \eta\Delta\Omega)/\eta a\tau$  and  $K_v = (E - E_v + \eta\Delta\Omega - \lambda\eta s_z)/\eta a\tau$ , where  $E_c$  ( $E_v$ ) is the energy of the conduction (valence) band minimum (maximum) in the absence of CPL and spin-orbit coupling.  $\theta$  is the incidence angle relative to the  $x$  axis.

Using the continuity of the wave function at the boundaries of each region, the boundary conditions are obtained:

$$\Psi_1(x=0) = \Psi_2(x=0), \quad (5a)$$

$$\Psi_2(x=L) = \Psi_3(x=L), \quad (5b)$$

where  $\Psi_1$ ,  $\Psi_2$ , and  $\Psi_3$  represent the wave functions in the MoS<sub>2</sub> region (without CPL), optical modulation region, and WS<sub>2</sub> region (without CPL), respectively. The spin- and valley-dependent transmission probability can be calculated through the transfer-matrix method [37]:  $T_{\eta,s} = |t_{\eta,s}|^2$ . The conductance at zero temperature is given by the Landauer-Büttiker formula [38]:

$$G_{\eta,s} = G_0 \int T_{\eta,s} \cos\theta d\theta, \quad (6)$$

where  $G_0 = 2e^2/h$  is the quantum conductance. Conductance of different spin and valley indices is denoted by  $G_{\uparrow,K}$ ,  $G_{\uparrow,K'}$ ,  $G_{\downarrow,K}$ ,  $G_{\downarrow,K'}$ , so the valley-resolved conductance and total conductance are

$$G_{K(K')} = \frac{G_{\uparrow,K(K')} + G_{\downarrow,K(K')}}{2}, \quad (7)$$

$$G_t = G_K + G_{K'}, \quad (8)$$

and the valley polarization is defined as

$$P_V = (G_K - G_{K'})/G_t. \quad (9)$$

### III. RESULTS AND DISCUSSION

#### A. Band structure

From Eq. (4), we can derive the energy dispersion of WS<sub>2</sub> and MoS<sub>2</sub> with CPL:

$$2E = \pm \sqrt{(2ka\tau)^2 + (E_c - E_v - \lambda\eta s + 2\eta\Delta\Omega)^2} + \lambda\eta s + E_c + E_v. \quad (10)$$

The effective energy of CPL ( $\Delta\Omega$ ) is coupled with valley index  $\eta$  in the dispersion. Figure 2 shows the electronic structure of monolayer TMDC in different valleys. When illuminated by off-resonant right-handed CPL, conduction-band electrons from  $K$  valley move to a high energy level, while those from  $K'$  valley become of lower energy.

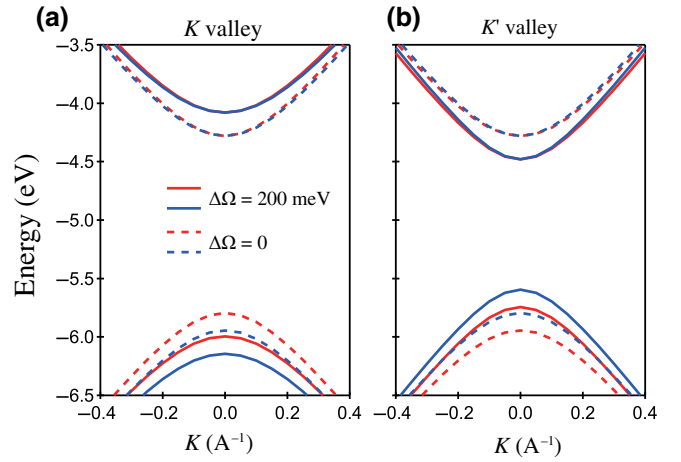


FIG. 2. Band structure of  $K$  valley (a) and  $K'$  valley (b) with  $\Delta\Omega = 200$  meV (solid lines) and  $\Delta\Omega = 0$  (dotted lines). Red and blue lines denote the spin-up and spin-down branches, respectively.

From Eq. (10), the CBM in the optically modulated region changes to  $E'_c = E_c + \Delta\Omega$  for  $K$  valley and  $E'_c = E_c - \Delta\Omega$  for  $K'$  valley [see Figs. 1(b) and 1(d)], where  $E_c$  represents the CBM of pristine monolayer MoS<sub>2</sub> or WS<sub>2</sub> obtained by first principles calculations [24]. In particular, when  $\Delta\Omega > \Delta\Omega_c = E_{c,WS_2} - E_{c,MoS_2}$ , the CPL-induced energy shift flips the original band offset. Therefore, the effective potentials in both Type-1 and Type-2 heterojunctions are spin and valley dependent, which leads to unique transmission when electrons tunnel through them.

#### B. Transmission, conductance, and polarization

In this section, we investigate the effect of CPL on spin and valley transport in the two types of planar heterojunctions. In Fig. 3, we depict transmission as a function of incidence angle and energy in Type-1 heterojunction. In the absence of CPL, electrons with the same value of  $\eta \times s$  are degenerate and have the same transmission properties. Especially, the transmission spectrum is separated at relatively large incidence angles ( $40^\circ$ ) due to the SOC-induced energy split in the conduction band [see Figs. 3(b3) and 3(b4)]. Now we are interested in the influence of right-handed CPL on the system. When tunneling from MoS<sub>2</sub> to WS<sub>2</sub>, electrons experience an effective potential barrier due to the positive band offset between WS<sub>2</sub> and MoS<sub>2</sub> [see Fig. 1(b)]. Only electrons with energy higher than  $E_{c,WS_2}$  can tunnel through the junction. The degeneracy of valley index is decreased by the right-handed CPL where  $K$  electrons need to overcome a higher potential barrier. This results in strong suppression of  $K$  valley electrons in transmission spectra [see Fig. 3(b5)]. Electrons with different spin are also separated in transmission due to the strong spin-valley coupling in TMDCs. In addition, the transmission probability of  $K$  electrons oscillates as incidence

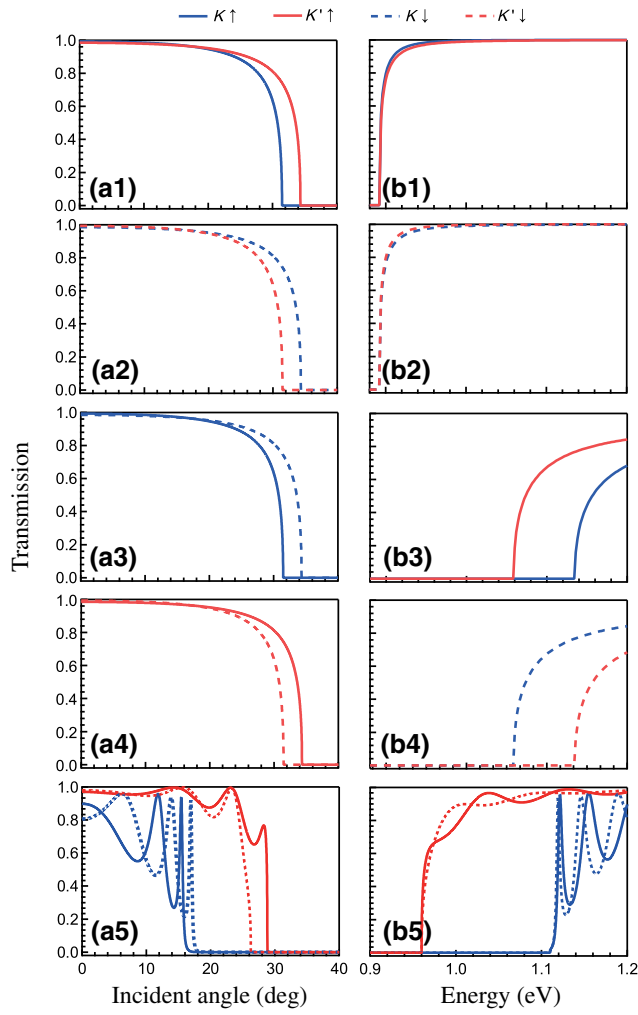


FIG. 3. Spin and valley transmission in Type-1 heterojunction. Transmission probability with respect to incidence angle when (a1)–(a4)  $\Delta\Omega = 0$  and (a5)  $\Delta\Omega = 150$  meV. Incidence energy is fixed at 1.2 eV above the Fermi energy. Transmission probability as a function of incidence energy at (b1)–(b4)  $\Delta\Omega = 0$  and (b5)  $\Delta\Omega = 200$  meV. Incidence angle is set to  $0^\circ$  in (b1), (b2), (b5) and  $40^\circ$  in (b3), (b4).

angle changes, and the cutoff incidence angle is smaller than that of  $K'$  electrons, which can be ascribed to the valley-dependent effective potential.

However, things are quite different in the Type-2 heterojunction, as can be seen in Fig. 4. First of all, transmission of electrons with a common  $\eta \times s$  is exactly the same [see Figs. 4(a), 4(b), 4(e), and 4(f)]. The higher cutoff energy of transmission than that of Type-1 is the result of higher  $E_c$  of  $\text{WS}_2$ . Surprisingly, transmission probability as a function of  $\Delta\Omega$  is strongly dependent on the relationship between  $\Delta\Omega$  and  $\Delta\Omega_c$ . When  $\Delta\Omega < \Delta\Omega_c$ , the transmission shows relatively less spin and valley dependence, and electrons with any incidence angle from  $0^\circ$  to  $90^\circ$  can tunnel through the heterojunction, which is quite different from that in the Type-1 heterojunction. This can be

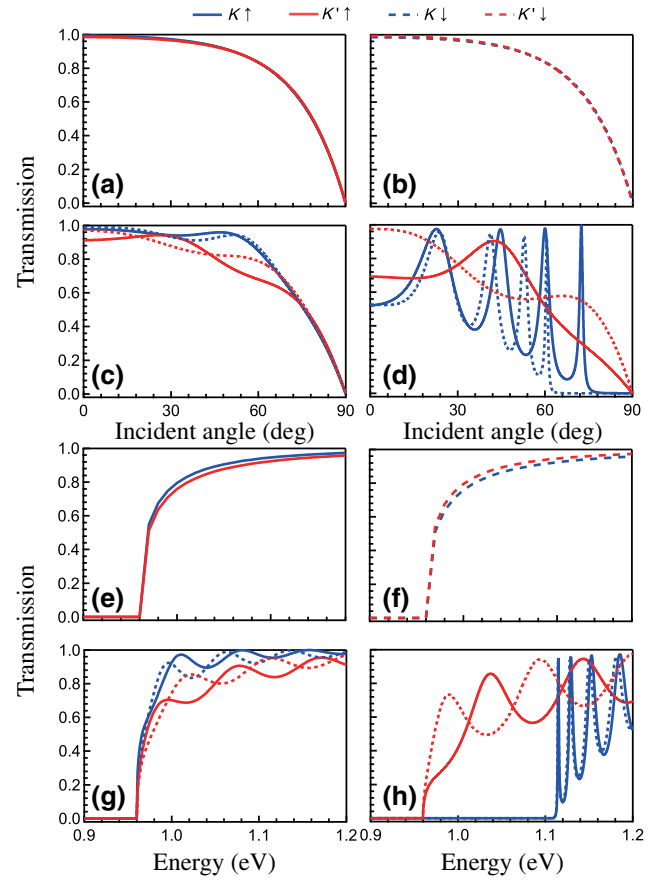


FIG. 4. Spin and valley transmission in Type-2 heterojunction. (a)–(d) Transmission probability with respect to incidence angle. Energy is fixed at 1.2 eV above the Fermi energy. (e)–(h) Transmission probability as a function of incidence energy. Incidence angle is set at  $0^\circ$  for all situations.  $\Delta\Omega = 0$  in (a), (b), (e), (f);  $\Delta\Omega = 150$  meV in (c), (g);  $\Delta\Omega = 500$  meV in (d), (h).

explained by the effective potential in the Type-2 heterojunction [see Fig. 1(d)]. The negative band offset between  $\text{MoS}_2$  and  $\text{WS}_2$  contributes an effective quantum well in the system, and electrons can tunnel through the junction with any incidence angle. When  $\Delta\Omega < \Delta\Omega_c$ , electrons from the  $K$  valley possess higher transmission probability than those in the Type-1 heterojunction. However, with increased  $\Delta\Omega$  ( $\Delta\Omega > \Delta\Omega_c$ ), transmission for the  $K$  valley is strongly suppressed. Transmission probability of  $K$  electrons as a function of incidence angle is split into several peaks [see Fig. 4(d)], and the allowed incidence angle of the  $K$  valley is limited, while there is no restriction on the incidence angle of  $K'$  electrons. With enhanced right-handed CPL intensity, the conduction band of  $K$  valley is modulated to higher energy, so the effective potential for  $K$  electrons changes into a barrier depending on angle and  $\Delta\Omega$ , which leads to great suppression of transmission for  $K$  valley in low-energy regions [see Fig. 4(h)]. The peaks in the transmission spectra of  $K$  electrons at high-energy

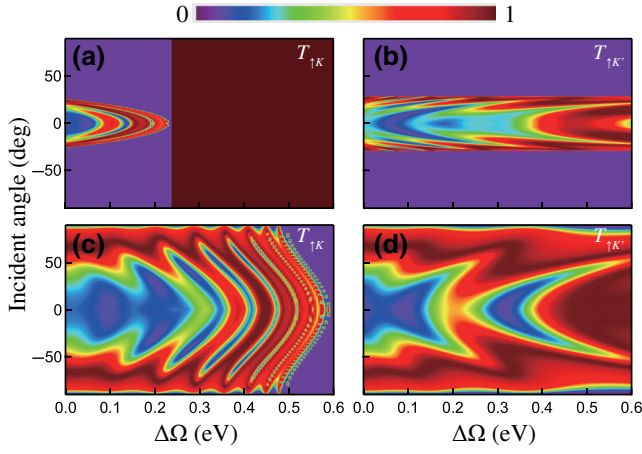


FIG. 5. Contour plot of transmission probability with respect to  $\theta$  and  $\Delta\Omega$ . Transmission of (a)  $K$  valley and (b)  $K'$  valley in Type-1 heterojunction (spin up). Transmission of (c)  $K$  valley and (d)  $K'$  valley in Type-2 heterojunction (spin up).

regions can be ascribed to the effective quantum well when  $x > L$ .

Figure 5 shows the influence of incidence angle and CPL intensity on the transmission. Obviously, for  $K$  valley electrons, the transmission is more suppressed in Type-1 than in Type-2 heterojunction, which originates from the different effective potential induced by band offsets and CPL. For example, for  $K$  valley electrons, as  $\Delta\Omega$  increases, the effective potential barrier crosses over the incidence energy, while the effective potential is always a quantum well for  $K'$  valley when  $\Delta\Omega > 0$ .

We further analyze the spin- and valley-resolved conductance in the two heterojunctions. Figures 6(a) and 6(b) show the conductance of different spins and valleys in Type-1 heterojunction.  $G_K$  is suppressed at low-energy region due to the right-handed-CPL-induced effective potential barrier. As the CPL intensity increases, the suppression effect is enhanced. Similar to the transmission spectra, the conductance of Type-2 heterojunction changes radically with  $\Delta\Omega$ . When  $\Delta\Omega < \Delta\Omega_c$ , the conductance of different valleys is similar in Fig. 6(c), where  $G_K$  is slightly higher than  $G_{K'}$ . While  $G_K$  decreases to zero in low-energy region when  $\Delta\Omega < \Delta\Omega_c$  because of the suppressed transmission. The peaks in  $G_K$  and oscillation in  $G_{K'}$  also originate from the transmission [see Fig. 6(d)].

Realization of spin or valley polarization is of great value in spintronics or valleytronics. Here we discuss the valley polarization in the two heterojunctions. We present valley polarization as a function of  $\Delta\Omega$  and  $L$  in Fig. 7. Perfect valley polarization platforms are observed in both types of heterojunctions. The valley polarization in Type-1 heterojunction changes from +100% to -100% monotonically when  $\Delta\Omega$  increases. Moreover, as the Fermi energy decreases, the value of  $\Delta\Omega$  needed to flip

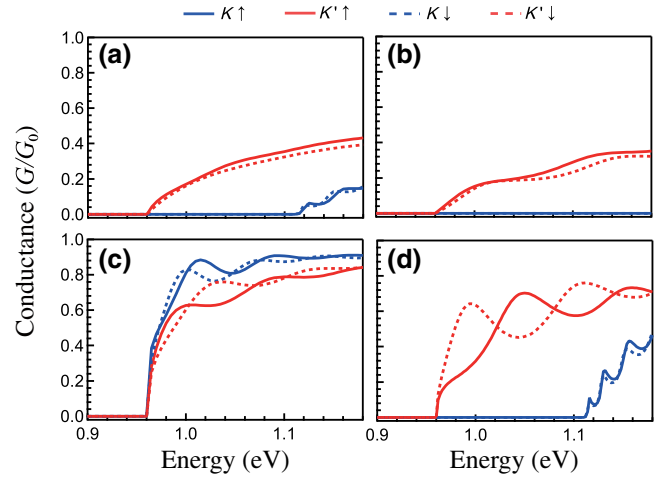


FIG. 6. Valley- and spin-resolved conductance ( $G/G_0$ ) in Type-1 (a),(b) and Type-2 (c),(d) heterojunctions.  $\Delta\Omega = 150$  meV in (a),(c);  $\Delta\Omega = 500$  meV in (b),(d).

the valley polarization is decreased as well [see black and green solid lines in Fig. 7(a)], which means the valley polarization can be fully controlled by relatively weak CPL. This benefits the application for a valley filter device. However, the strong valley polarization in Type-2 heterojunction is only realized at large  $\Delta\Omega$  ( $\Delta\Omega > \Delta\Omega_c$ ), while the valley polarization is very weak when  $\Delta\Omega < \Delta\Omega_c$  [see Fig. 7(b)]. If we denote perfect valley polarization as “on” state and nearly nonpolarized valley transport as “off” state [see the red and blue shading in Fig. 7(b)], the Type-2 heterojunction may be applied to a valley transistor controlled by CPL, where the valley polarization transport state can be turned on or off only by the helicity and intensity of CPL.

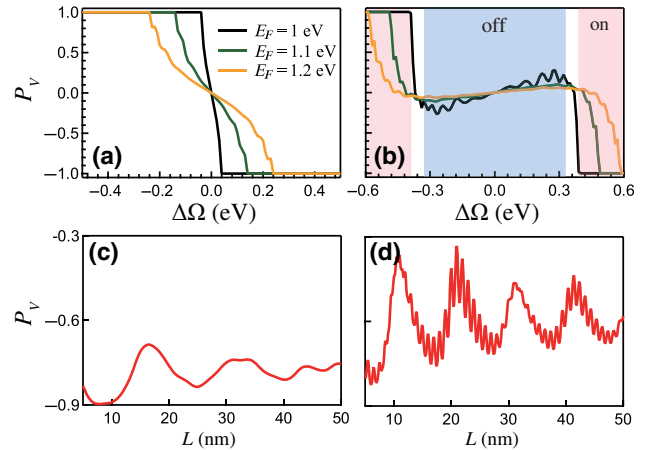


FIG. 7. Valley polarization ( $P_V$ ) as a function of CPL intensity and length of modulation region (a),(c) for Type-1 heterojunction and (b),(d) for Type-2 heterojunction.  $\Delta\Omega = 35$  meV in (c) and  $\Delta\Omega = 385$  meV in (d).

We also investigate the robustness of valley polarization as a function of the length of the modulation region  $L$ . As can be seen from Figs. 7(c) and 7(d), the valley polarization in both types of heterojunctions oscillates with  $L$ .  $P_V$  remains negative when  $L$  increases, which can be explained by the effective quantum well for  $K'$  valley electrons in both types of heterojunctions. The oscillation amplitude in Type-1 is smaller than that in Type-2 due to the stronger suppression of  $K$  valley transport in Type-1 heterojunction, so the valley polarization in Type-1 heterojunction is relatively robust when the size of the modulation region changes.

It should be pointed out that for other TMDC PHs with common  $X$  atom, such as  $\text{MoSe}_2/\text{WSe}_2$ , the CBM and valence band maximum of  $\text{WX}_2$  are higher than those of  $\text{MoX}_2$  [24]. For example, the CBM of  $\text{WS}_2$  is 0.35 eV higher than that of  $\text{MoS}_2$  ( $\Delta\Omega_c = 0.35$  eV), while in the  $\text{MoSe}_2/\text{WSe}_2$  PHs,  $\Delta\Omega_c = 0.3$  eV. In the two typical TMDC materials  $\text{MoSe}_2$  and  $\text{MoS}_2$ , the band gap and SOC strength are almost the same, and so are in  $\text{WSe}_2$  and  $\text{WS}_2$ . When the optical modulation with appropriate intensity is applied, the off-resonant CPL modifies the band structure and the relative CBM energy offsets in the two types of  $\text{MoSe}_2/\text{WSe}_2$  PHs are similar to those in the  $\text{MoS}_2/\text{WS}_2$  PHs. Therefore, the spin- and valley-resolved transmission and conductance in the  $\text{MoS}_2/\text{WS}_2$  and  $\text{MoSe}_2/\text{WSe}_2$  PHs are qualitatively similar. The numerical results show that there are only some quantitative differences between the quantum transport and valley polarization under optical modulation in the  $\text{MoS}_2/\text{WS}_2$  and  $\text{MoSe}_2/\text{WSe}_2$  PHs. The main results obtained for the  $\text{MoS}_2/\text{WS}_2$  PHs hold well for other TMDC PHs with common  $X$  atom.

#### IV. CONCLUSION

In summary, we systematically explore the quantum transport properties of two different structures of TMDC planar heterojunctions modulated by off-resonant circularly polarized light. Interestingly, the spin- and valley-resolved transmission of the two types of heterojunctions are quite different due to the band offset and CPL-induced effective potential. Specifically, in the Type-1 heterojunction, the  $K$  valley transmission is extremely suppressed at low energy and behaves as peaks in the spectrum, which leads to perfect valley polarization. And the allowed incidence angle of  $K$  electrons is more limited than that of  $K'$  electrons. However, the transmission in the Type-2 heterojunction depends strongly on CPL intensity. When  $\Delta\Omega < \Delta\Omega_c$ , the transmission probability of electrons from both valleys share common cutoff energy and the polarization is very weak. There is no restriction on incidence angle in the transmission of Type-2 heterojunction. While under relatively strong CPL ( $\Delta\Omega > \Delta\Omega_c$ ), the  $K$  valley transmission is suppressed again and changes into several peaks in the spectrum, and the valley polarization recovers

to 100% or  $-100\%$ . With these results, we theoretically propose a pure optically controlled valley filter and valley transistor based on the two types of planar heterojunctions, respectively. Our work may be useful for design and application of photovallelytronic devices based on TMDC planar heterojunctions.

#### ACKNOWLEDGMENTS

This work is supported by the National Natural Science Foundation of China under Grant No. 12074209.

- [1] K. S. Novoselov, D. Jiang, F. Schedin, T. J. Booth, V. V. Khotkevich, S. V. Morozov, and A. K. Geim, Two-dimensional atomic crystals, *Proc. Natl. Acad. Sci. U. S. A.* **102**, 10451 (2005).
- [2] C. Lee, Q. Li, W. Kalb, X. Z. Liu, H. Berger, R. W. Carpick, and J. Hone, Frictional characteristics of atomically thin sheets, *Science* **328**, 76 (2010).
- [3] A. Splendiani, L. Sun, Y. Zhang, T. Li, J. Kim, C. Y. Chim, G. Galli, and F. Wang, Emerging photoluminescence in monolayer  $\text{MoS}_2$ , *Nano Lett.* **10**, 1271 (2010).
- [4] K. F. Mak, C. Lee, J. Hone, J. Shan, and T. F. Heinz, Atomically Thin  $\text{MoS}_2$ : A New Direct-Gap Semiconductor, *Phys. Rev. Lett.* **105**, 136805 (2010).
- [5] D. Xiao, G. B. Liu, W. Feng, X. Xu, and W. Yao, Coupled Spin and Valley Physics in Monolayers of  $\text{MoS}_2$  and Other Group-VI Dichalcogenides, *Phys. Rev. Lett.* **108**, 196802 (2012).
- [6] Z. Y. Zhu, Y. C. Cheng, and U. Schwingenschlöggl, Giant spin-orbit-induced spin splitting in two-dimensional transition-metal dichalcogenide semiconductors, *Phys. Rev. B* **84**, 153402 (2011).
- [7] T. Li and G. Galli, Electronic properties of  $\text{MoS}_2$  nanoparticles, *J. Phys. Chem. C* **111**, 16192 (2007).
- [8] S. Lebegue and O. Eriksson, Electronic structure of two-dimensional crystals from ab initio theory, *Phys. Rev. B* **79**, 115409 (2009).
- [9] L. L. Tao, A. Naeemi, and E. Y. Tsybmal, Valley-Spin Logic Gates, *Phys. Rev. Appl.* **13**, 054043 (2020).
- [10] W. T. Lu, H. Y. Tian, H. M. Liu, Y. F. Li, and W. Li, Spin- and valley-dependent negative magnetoresistance in a ferromagnetic  $\text{MoS}_2$  junction with a quantum well, *Phys. Rev. B* **98**, 075405 (2018).
- [11] X. J. Qiu, Z. Z. Cao, J. Hou, and C. Y. Yang, Controlled giant magnetoresistance and spin-valley transport in an asymmetrical  $\text{MoS}_2$  tunnel junction, *Appl. Phys. Lett.* **117**, 102401 (2020).
- [12] K. Hao, G. Moody, F. Wu, C. K. Dass, L. Xu, C. H. Chen, L. Sun, M. Y. Li, L. J. Li, A. H. MacDonald, and X. Li, Direct measurement of exciton valley coherence in monolayer  $\text{WSe}_2$ , *Nat. Phys.* **12**, 677 (2016).
- [13] M. Tahir, A. Manchon, and U. Schwingenschlöggl, Photoinduced quantum spin and valley Hall effects, and orbital magnetization in monolayer  $\text{MoS}_2$ , *Phys. Rev. B* **90**, 125438 (2014).
- [14] T. Cao, G. Wang, W. Han, H. Ye, C. Zhu, J. Shi, Q. Niu, P. Tan, E. Wang, B. Liu, and J. Feng, Valley-selective

- circular dichroism of monolayer molybdenum disulphide, *Nat. Commun.* **3**, 887 (2012).
- [15] K. F. Mak, K. He, and T. F. Heinz, Control of valley polarization in monolayer MoS<sub>2</sub> by optical helicity, *Nat. Nanotechnol.* **7**, 494 (2012).
- [16] H. Zeng, J. Dai, W. Yao, D. Xiao, and X. Cui, Valley polarization in MoS<sub>2</sub> monolayers by optical pumping, *Nat. Nanotechnol.* **7**, 490 (2012).
- [17] C. Park, Magnetoelectrically Controlled Valley Filter and Valley Valve in Bilayer Graphene, *Phys. Rev. Appl.* **11**, 044033 (2019).
- [18] D. N. Liu, B. Y. Liu, R. Y. Yuan, J. Zheng, and Y. Guo, Valley filter and valley valve based on WSe<sub>2</sub> double-barrier junctions modulated by polarized light, *Phys. Rev. B* **103**, 245432 (2021).
- [19] D. Zambrano, P. Orellana, L. Rosales, and A. Latgé, Spin and Valley Filter Based on Two-Dimensional WSe<sub>2</sub> Heterostructures, *Phys. Rev. Appl.* **15**, 034069 (2021).
- [20] Y. An, M. Zhang, D. Wu, T. Wang, Z. Jiao, C. Xia, Z. Fu, and K. Wang, The rectifying and negative differential resistance effects in graphene/h-BN nanoribbon heterojunctions, *Phys. Chem. Chem. Phys.* **18**, 27976 (2016).
- [21] Y. W. Son, M. L. Cohen, and S. G. Louie, Energy Gaps in Graphene Nanoribbons, *Phys. Rev. Lett.* **97**, 216803 (2006).
- [22] M. Y. Han, B. Özyilmaz, Y. Zhang, and P. Kim, Energy Band-Gap Engineering of Graphene Nanoribbons, *Phys. Rev. Lett.* **98**, 206805 (2007).
- [23] O. Ávalos-Ovando, D. Mastrogiuseppe, and S. E. Ulloa, Lateral interfaces of transition metal dichalcogenides: A stable tunable one-dimensional physics platform, *Phys. Rev. B* **99**, 035107 (2019).
- [24] J. Kang, S. Tongay, J. Zhou, J. Li, and J. Wu, Band offsets and heterostructures of two-dimensional semiconductors, *Appl. Phys. Lett.* **102**, 012111 (2013).
- [25] H. Ghadiri and A. Saffarzadeh, Band-offset-induced lateral shift of valley electrons in ferromagnetic MoS<sub>2</sub>/WS<sub>2</sub> planar heterojunctions, *J. Appl. Phys.* **123**, 104301 (2018).
- [26] J. Lee, J. Huang, B. G. Sumpter, and M. Yoon, Strain-engineered optoelectronic properties of 2D transition metal dichalcogenide lateral heterostructures, *2D Mater.* **4**, 021016 (2017).
- [27] Z. Zhang, Y. Xie, Q. Peng, and Y. Chen, A theoretical prediction of super high-performance thermoelectric materials based on MoS<sub>2</sub>/WS<sub>2</sub> hybrid nanoribbons, *Sci. Rep.* **6**, 21639 (2016).
- [28] X. Duan, C. Wang, J. C. Shaw, R. Cheng, Y. Chen, H. Li, X. Wu, Y. Tang, Q. Zhang, A. Pan, J. Jiang, R. Yu, Y. Huang, and X. Duan, Lateral epitaxial growth of two-dimensional layered semiconductor heterojunctions, *Nat. Nanotechnol.* **9**, 1024 (2014).
- [29] Y. Gong, J. Lin, X. Wang, G. Shi, S. Lei, Z. Lin, X. Zou, G. Ye, R. Vajtai, B. I. Yakobson, H. Terrones, M. Terrones, B. K. Tay, J. Lou, S. T. Pantelides, Z. Liu, W. Zhou, and P. M. Ajayan, Vertical and in-plane heterostructures from WS<sub>2</sub>/MoS<sub>2</sub> monolayers, *Nat. Mater.* **13**, 1135 (2014).
- [30] K. Chen, X. Wan, W. Xie, J. Wen, Z. Kang, X. Zeng, H. Chen, and J. Xu, Lateral built-in potential of monolayer MoS<sub>2</sub>-WS<sub>2</sub> in-plane heterostructures by a shortcut growth strategy, *Adv. Mater.* **27**, 6431 (2015).
- [31] C. Huang, S. Wu, A. M. Sanchez, J. J. P. Peters, R. Beanland, J. S. Ross, P. Rivera, W. Yao, D. H. Cobden, and X. Xu, Lateral heterojunctions within monolayer MoSe<sub>2</sub>-WSe<sub>2</sub> semiconductors, *Nat. Mater.* **13**, 1096 (2014).
- [32] P. K. Sahoo, S. Memaran, Y. Xin, L. Balicas, and H. R. Gutiérrez, One-pot growth of two-dimensional lateral heterostructures via sequential edge-epitaxy, *Nature* **553**, 63 (2018).
- [33] C. Zhang, M. Y. Li, J. Tersoff, Y. Han, Y. Su, L. J. Li, D. A. Muller, and C. K. Shih, Strain distributions and their influence on electronic structures of WSe<sub>2</sub> – MoS<sub>2</sub> laterally strained heterojunctions, *Nat. Nanotechnol.* **13**, 152 (2018).
- [34] B. Dóra, J. Cayssol, F. Simon, and R. Moessner, Optically Engineering the Topological Properties of a Spin Hall Insulator, *Phys. Rev. Lett.* **108**, 056602 (2012).
- [35] M. Ezawa, Photoinduced Topological Phase Transition and a Single Dirac-Cone State in Silicene, *Phys. Rev. Lett.* **110**, 026603 (2013).
- [36] T. Kitagawa, T. Oka, A. Brataas, L. Fu, and E. Demler, Transport properties of nonequilibrium systems under the application of light: Photoinduced quantum Hall insulators without Landau levels, *Phys. Rev. B* **84**, 235108 (2011).
- [37] D. Y. K. Ko and J. C. Inkson, Matrix method for tunneling in heterostructures: Resonant tunneling in multilayer systems, *Phys. Rev. B* **38**, 9945 (1988).
- [38] M. Büttiker, Four-Terminal Phase-Coherent Conductance, *Phys. Rev. Lett.* **57**, 1761 (1986).